PAPER

Check for updates

High-temperature calcination enhances the activity of MnOx catalysts for soot oxidation†

Meng Wang,[a] Jingyi Wang,[ac] Yan Zhang, [iD] *[ac] Yunbo Yu [iD] [bc] and Wenpo Shan*[ac]

High-temperature calcination usually induces the sintering of catalysts, thus resulting in negative effects on their performance. However, in this study we surprisingly found that high-temperature calcination could enhance the activity of MnOx catalysts for soot oxidation. Combined experimental and theoretical analysis revealed that high-temperature calcination of MnOx (900 °C) could induce the generation of more oxygen defects, due to the transformation of α-MnO$_2$ to δ-MnO$_2$ and Mn$_2$O$_3$, with lower formation energy for oxygen defects. The generated oxygen defects would facilitate activation of surface chemisorbed oxygen, producing more active oxygen species, which can further oxidize NO to NO$_2$ to accelerate soot combustion. Therefore, MnOx calcined at 900 °C exhibited much higher activity for soot oxidation than that calcined at 500 °C. This study provides significant insight into the effects of calcination temperature on MnOx catalysts, thereby aiding in the design of high-efficiency catalysts for the control of soot emission.

1. Introduction

With the growing awareness of the need for environmental protection and increasingly stringent emission regulations, air pollution and public health problems caused by diesel soot particles have attracted considerable attention.[1–5] The diesel particulate filter (DPF) is one of the most efficient solutions for soot control. However, soot accumulates on the DPF, which needs periodic regeneration. Otherwise, the backpressure created by the loaded DPF could potentially have a negative influence on the efficiency of the engine. There are two kinds of regeneration methods, which are active and passive regeneration. Active regeneration is *via* post injection of fuel to raise the DPF inlet gas temperature to boost soot combustion. Passive regeneration is *via* a soot oxidation catalyst coated in the DPF to lower the ignition temperature of soot.[6–8] Therefore, the development of high-efficiency soot oxidation catalysts is crucial.

Considerable numbers of catalytic materials for soot oxidation have been reported. Noble metal catalysts have gained a great deal of attention because of their excellent oxidation performance.[9] For instance, Wu *et al.* reported a Pt/H-ZSM-5 catalyst, which can decrease the T_{50} of soot oxidation from 570 °C to 440 °C, in comparison with uncatalyzed soot oxidation.[10] However, due to the high cost and low natural abundance of noble metals,[11,12] the search for economical catalysts as alternatives to noble metal catalysts has triggered growing interest. Mn oxides for soot catalytic oxidation have attracted great attention, due to their strong redox ability, abundant resources, inexpensive and environmental benefits. In Zhang's work,[13] it was found that the T_{50} of soot can been decreased from above 600 °C to 407 °C using α-MnO$_2$ as catalyst, which revealed that the α-MnO$_2$ catalyst had excellent soot oxidation performance. To further improve the soot catalytic oxidation activity of Mn oxides, combining MnOx with some other metals has been widely tried. Li *et al.* introduced Co into a manganese oxide octahedral molecular sieve (OMS-2), and the T_{50} of soot oxidation was decreased from 428 to 383 °C.[14] Jampaiah's work[15] found that the addition of Co and Cu to α-MnO$_2$ could generate more oxygen defects, which was beneficial to soot oxidation. As a result, the T_{50} of the 5Cu5Co–MnO$_2$ catalyst was decreased from 547 °C to 431 °C.

In addition, to meet diesel emission standards (China VI or EU VI), the DPF needs to combine active regeneration and passive regeneration. Therefore, the soot oxidation catalyst will periodically work in a high-temperature environment (even reaching 900 °C). Generally, high-temperature calcination has negative effects on the performance of Mn oxide catalysts. For example, Zhao's work found that when the calcination temperature was increased from 450 °C to

a Institute of Urban Environment, Chinese Academy of Sciences, Xiamen 361021, China. E-mail: yzhang3@iue.ac.cn, wpshan@iue.ac.cn; Tel: +86 574 86085855
b State Key Joint Laboratory of Environment Simulation and Pollution Control, Research Center for Eco-Environmental Sciences, Chinese Academy of Sciences, Beijing 100085, China
c University of Chinese Academy of Sciences, Beijing 100049, China

6278 | *Catal. Sci. Technol.*, 2024, **14**, 6278–6285

This journal is © The Royal Society of Chemistry 2024

850 °C, the T_{50} of the K-OMS-2 catalyst (cryptomelane-type $K_{2-x}Mn_8O_{16}$) increased from 336 °C to 377 °C.[16] Cui's work also found that the soot oxidation activity of a Mn_xCo_y porous nanosheet catalyst significantly decreased after calcining at 800 °C for 10 h, with the T_{50} increasing from 363 °C to about 450 °C.[17] However, in this work, it was interestingly found that high-temperature calcination at 900 °C could enhance the activity of a MnO_x catalyst prepared by a hydrothermal method for soot oxidation. A series of characterization experiments and density functional theory (DFT) calculations were carried out to investigate the promotional effects of high-temperature calcination.

2. Experimental

2.1 Catalyst preparation

MnO_x was prepared by a hydrothermal method.[2,18,19] 18.34 g of $MnAC_2·4H_2O$ was dissolved in deionized water under agitation, and 12.5 mL glacial acetic acid was added. Next, a solution of 10.84 g $KMnO_4$ was added slowly to the above mixture. Subsequently, the mixed solution was transferred into a 500 mL Teflon-lined autoclave, which was sealed and heated at 100 °C for 24 h. After cooling, a black slurry was obtained and washed with deionized water. The final sample was dried at 110 °C overnight, and the obtained product was named MnO_x. Finally, the MnO_x was calcined at 500 °C and 900 °C in air for 3 h and denoted as MnO_x-500 and MnO_x-900, respectively. The detailed preparation methods are described in the ESI.†

2.2 Catalyst characterization and DFT calculation

The catalysts were characterized via XRD, Raman, XPS, H_2-TPR, Soot-TPR, XAFS, EPR, and so on. DFT calculation was executed using the Vienna Ab initio Simulation Package (VASP). The detailed methods of catalyst characterization and DFT calculation are shown in the ESI.†

2.3 Evaluation of soot oxidation activity

The soot oxidation activity of the catalysts was measured via soot-TPO in a fixed-bed quartz tube reactor. For the soot oxidation activity test, the reactants included 10% O_2, 0.1% NO (when used), and 5% H_2O (when used) in N_2 balance. The outlet gas was detected with an Antaris IGS gas analyzer (Thermo Fisher). The details of the experiment are described in the ESI.†

3. Results and discussion

3.1 Catalytic activity and kinetic studies

The performance of soot without catalyst, and MnO_x-500 and MnO_x-900 catalysts for soot oxidation was evaluated under different reaction conditions, and the results are shown in Fig. 1a and b. Compared with the MnO_x-500 catalyst, the MnO_x-900 catalyst showed higher soot oxidation activity under 10% O_2 balanced by N_2, with the T_{50} lowered by about 38 °C (Fig. 1a). When 0.1% NO was introduced into the

reaction gases, the soot oxidation performance of MnO_x-500 and MnO_x-900 catalysts remarkably improved in both cases, and the MnO_x-900 catalyst, with T_{50} decreasing to 365 °C, still exhibited higher soot oxidation activity than MnO_x-500 (394 °C). In addition, it was worth noting that the MnO_x-900 catalyst also exhibited higher soot oxidation activity in the tight contact (Fig. S1a–c†). Five soot-TPO cycles were carried out to investigate the stability of the MnO_x-900 catalyst in the $NO/O_2/N_2$ atmosphere, and the results showed that the MnO_x-900 catalyst is stable for soot oxidation (Fig. 1c). Therefore, the MnO_x-900 catalyst has the most potential to be applied for efficiently eliminating soot emissions.

NO_2 is more active than O_2 in enhancing soot oxidation reactions.[9] Therefore, the evaluation of NO-to-NO_2 oxidation capacity on the MnO_x-500 and MnO_x-900 catalysts was performed, and NO_2 utilization efficiencies were calculated by eqn (S1).† As shown in Fig. 1d, the calculated NO_2 efficiency of the MnO_x-900 catalyst was much higher than that of the MnO_x-500 catalyst. This result indicated that high-temperature calcination of the catalyst can facilitate the participation of NO_2 in soot oxidation. In addition, as shown in Fig. S2,† with the calcination increasing from 500 to 900 °C, the contact efficiency of T_{90} increased from 0.77 to 0.89, which revealed that the high-temperature calcination was beneficial for improving the contact between soot and the catalyst.

The presence of water in the exhaust of diesel engines is unavoidable. Thus, to explore the soot oxidation performance of the MnO_x-900 catalyst under real conditions, 5% H_2O was introduced into the reaction gases. As shown in Fig. 2a, the T_{10}, T_{50} and T_{90} of MnO_x-900 have a slight change under the influence of H_2O, indicating high resistance to H_2O. Moreover, five soot-TPO cycles were performed in the $H_2O/NO/O_2/N_2$ atmosphere, and it was evident that MnO_x-900 was stable for soot oxidation (Fig. S1d†). To deeply investigate the intrinsic activity for soot oxidation, the activation energies of the two catalysts were measured by the Ozawa method, and the Ozawa plots and E_a values are shown in Fig. 2b. Clearly, the E_a value of MnO_x-900 (61.5 kJ mol^{-1}) was smaller than that of MnO_x-500 (66.2 kJ mol^{-1}), which suggested that high-temperature calcination can improve the intrinsic catalytic activity of the MnO_x catalyst.

3.2 Structural properties

The XRD patterns of the MnO_x-500 and MnO_x-900 catalysts are shown in Fig. 3a. MnO_x-500 only displayed the characteristic peaks of α-MnO_2 (PDF#44-0141). When the calcination temperature of MnO_x increased to 900 °C, the diffraction peaks of δ-MnO_2 and Mn_2O_3 were observed,[20,21] indicating that α-MnO_2 transformed into δ-MnO_2 and Mn_2O_3 due to high-temperature calcination. DTG was also used to explore the effect of calcination temperature on the MnO_x catalyst. As shown in Fig. 3b, three peaks with associated weight losses were observed, centered at 626 °C, 857 °C, and 892 °C. Based on previous reports,[22,23] the first peak was
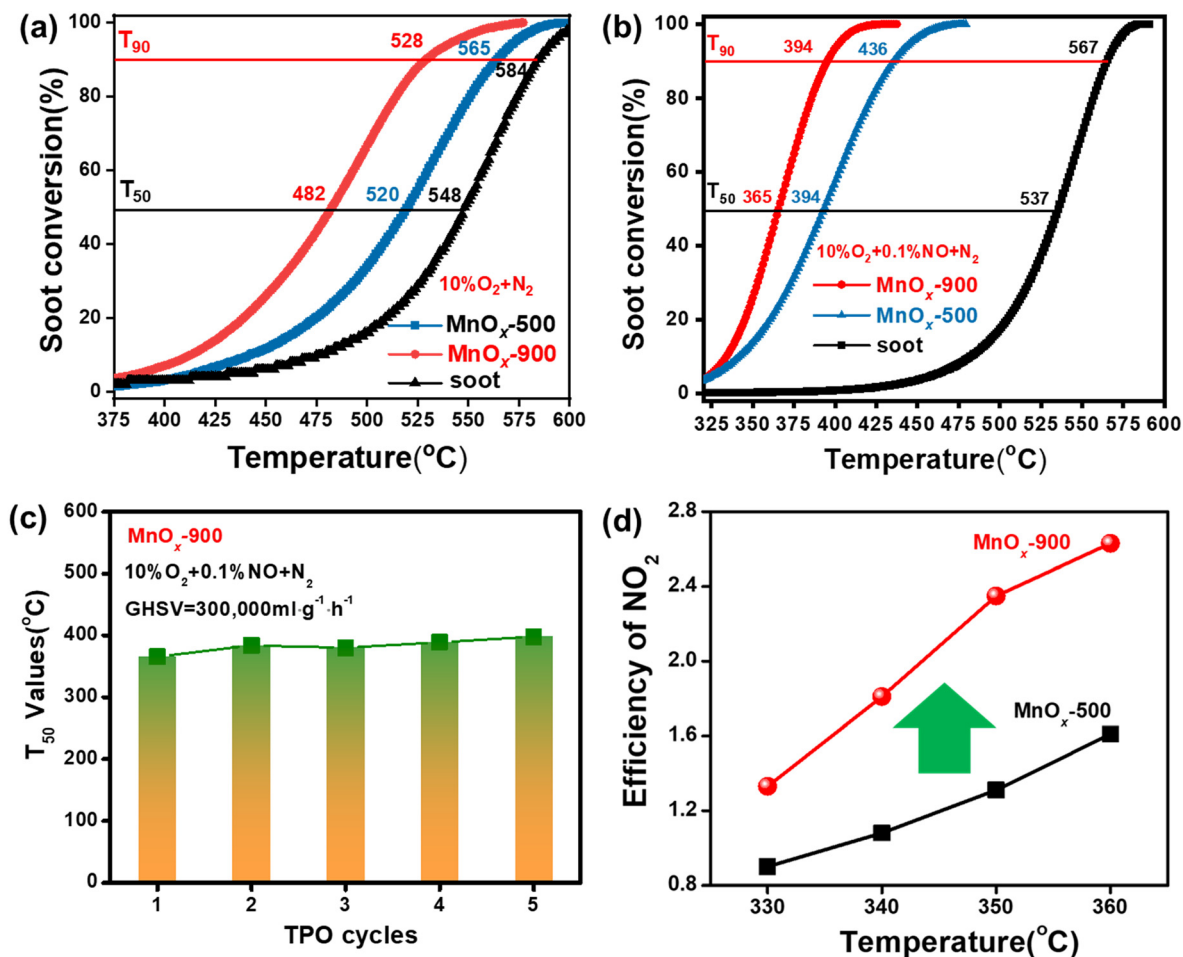
Fig. 1 Soot conversion over the MnO_x-500 and MnO_x-900 catalysts (a and b), the stability of the MnO_x-900 catalyst in five soot-TPO cycles (c), and the utilization efficiency of NO_2 at different temperatures over the MnO_x-500 and MnO_x-900 catalysts (d). Reaction conditions: 0.1% NO (when used), 10% O_2 balanced by N_2 under loose contact and heating rate = 2 °C min^{-1}.
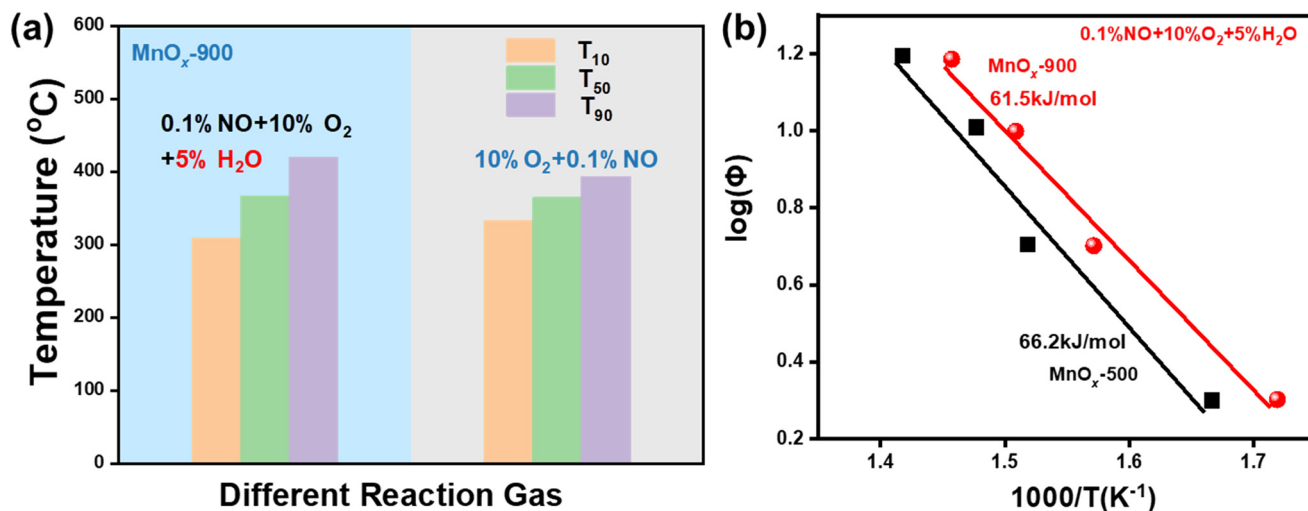

Fig. 2 T_{10}, T_{50} and T_{90} of the MnO_x-900 catalyst under different reaction conditions (a), and Ozawa plots for 10% soot conversion of the MnO_x-500 and MnO_x-900 catalysts with varying temperature increase rates of 2, 5, 10, and 15 °C min^{-1}, under loose contact. Feed composition: 0.1% NO, 5% H_2O, 10% O_2, and N_2 balance (b).
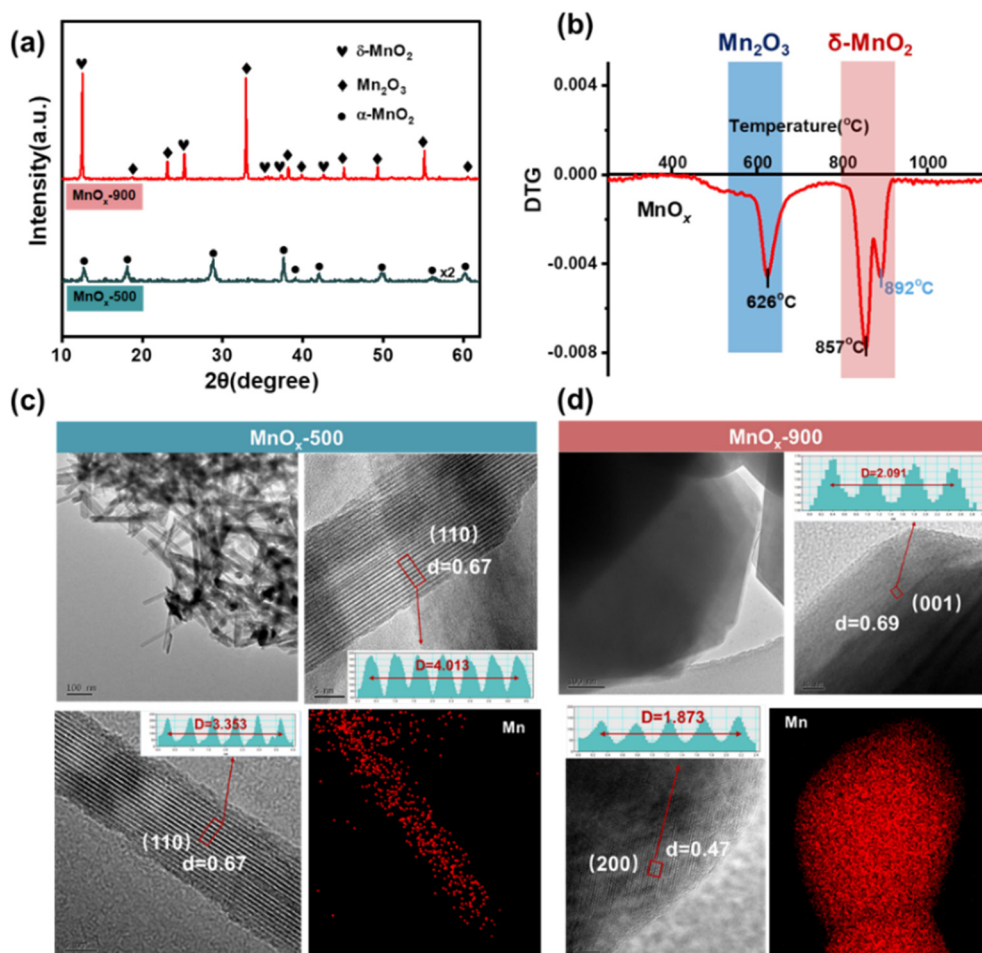
Fig. 3 XRD patterns for the MnO_x-500 and MnO_x-900 catalysts (a), the DTG profile of MnO_x (b), and TEM and HRTEM images over the MnO_x-500 and MnO_x-900 catalysts (c and d).

related to the formation of Mn_2O_3, and the other peaks were due to the appearance of δ-MnO_2, which was further confirmed by the XRD results. Fig. 3c and d shows the TEM and HRTEM images of the MnO_x-500 and MnO_x-900 catalysts. As shown in Fig. 3c, MnO_x-500 exhibited a nanorod structure, and clear lattice fringes were observed, which can be assigned to the (110) planes of α-MnO_2. Fig. 3d revealed that the lattice fringe spacing of MnO_x-900 was 0.697 nm and 0.468 nm, corresponding to the (001) plane of δ-MnO_2 and the (200) plane of the Mn_2O_3, which was consistent with the XRD results. In addition, the pore parameters and BET surface areas are shown in Table S1.† It is noted that MnO_x-900 possessed a smaller specific surface area (3.1 m^2 g^{-1}) than that of MnO_x-500 (61.4 m^2 g^{-1}), which could be due to high temperature calcination leading to the collapse of stacked pores.

3.3 Oxygen defects

Oxygen defects play a key role in oxidation reactions, which are beneficial to the activation of gaseous oxygen. To further investigate the influence of calcination temperature on the

oxygen defects of the catalysts, Raman, EPR, and XAFS spectroscopy, and DFT calculations were carried out, and the results are shown in Fig. 4. Fig. 4a displays the Raman spectra of the MnO_x-500 and MnO_x-900 catalysts. The peak of the MnO_x-500 catalyst located at 661 cm^{-1} was assigned to the symmetric stretching vibration of the Mn–O bond.[14,24–26] Interestingly, when the calcination temperature was increased to 900 °C, the peak shifted to 655 cm^{-1}, indicating that the strength of the Mn–O bond was weakened (Hooke's law[27,28]). The weak Mn–O bond would be beneficial to the formation of oxygen defects.[27] In addition, the relative intensity of the Raman peak is related to number of oxygen defects.[14,26,29] With the calcination temperature increasing to 900 °C, the intensity of the Raman peak was clearly strengthened, suggesting that the generation of oxygen defects was clearly promoted on MnO_x-900 due to high-temperature calcination.

EPR was also used to analyze the oxygen defects of the catalysts. As shown in Fig. 4b, both the MnO_x-500 and MnO_x-900 catalysts exhibited a symmetrical EPR signal at g = 2.004, indicating the existence of oxygen defects.[30–32] Interestingly, as the calcination temperature increased, the signal intensity
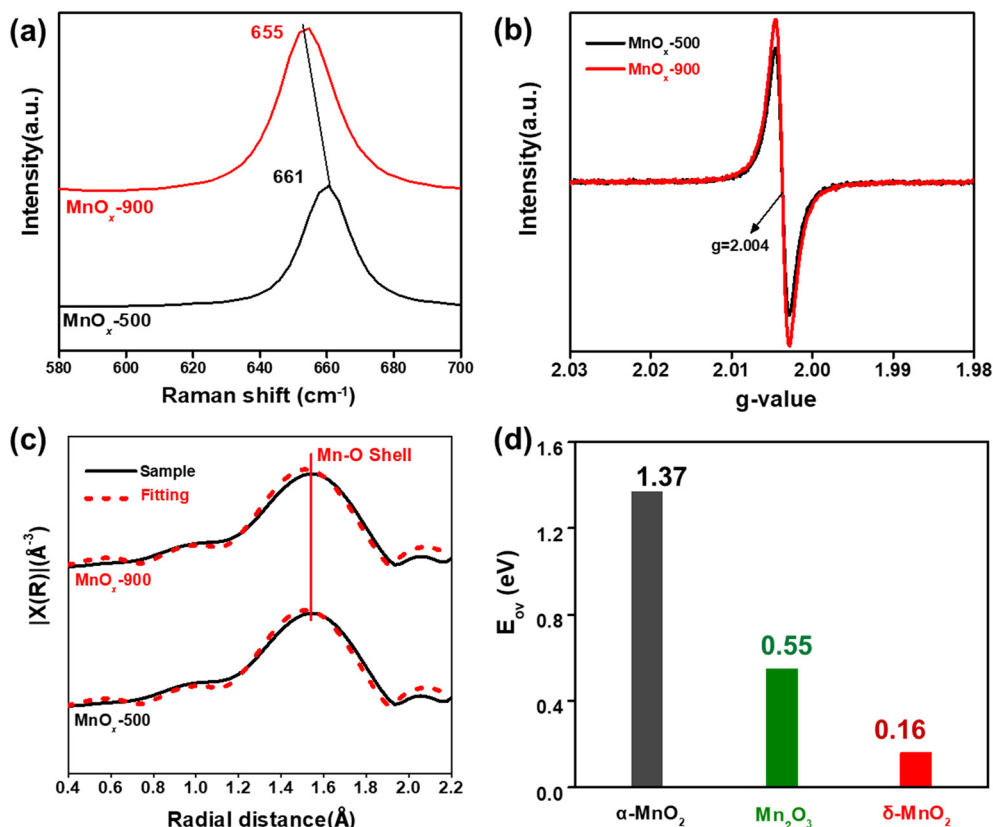
This journal is © The Royal Society of Chemistry 2024

Catal. Sci. Technol., 2024, **14**, 6278–6285 | **6281**

Fig. 4 The Raman (a), EPR (b), and XAFS (c) results of the MnO_x-500 and MnO_x-900 catalysts, and the formation energy of oxygen vacancies over the α-MnO_2, Mn_2O_3 and δ-MnO_2 surfaces (d).

of the oxygen defect peak was enhanced, indicating an increase in the number of oxygen defects on the MnO_x-900 catalyst.[29] Moreover, Mn K-edge EXAFS spectroscopy was carried out to further evaluate the oxygen defects of the MnO_x-500 and MnO_x-900 catalysts. Compared with the MnO_x-500 catalyst, the coordination numbers of the Mn–O shell decreased for the MnO_x-900 catalyst, confirming that high-temperature calcination was beneficial to the generation of more oxygen defects (Fig. 4c and Table S2†).[33,34] In addition, the oxygen vacancy formation energy of the α-MnO_2, δ-MnO_2 and Mn_2O_3 catalysts was calculated using DFT, and the results are shown in Fig. 4d. The formation energies of oxygen defects on δ-MnO_2 and Mn_2O_3 were both lower than that on α-MnO_2. According to the XRD and DTG results, high-temperature calcination can induce the transformation of α-MnO_2 to δ-MnO_2 and Mn_2O_3 in the MnO_x catalyst. Therefore, the DFT calculation results indicated that the formation of oxygen defects on MnO_x-900 is easier than that on MnO_x-500, which is consistent with the Raman, EPR and EXAFS results.

3.4 Characterization of the active oxygen species

Oxygen species play a key role in the soot oxidation reaction. To analyze the chemical state of the oxygen species, the O 1s XPS spectra of the MnO_x-500 and MnO_x-900 catalysts were measured. As shown in Fig. 5a, three kinds of oxygen species could be observed for both the MnO_x-500 and MnO_x-900 catalysts. The peaks centered at 528.9–530.1 eV, 530–531 eV, and 532 eV were assigned to lattice oxygen species (O_β), surface adsorbed oxygen species (O_α), and surface adsorbed H_2O (O_γ), respectively.[35–37] It has been reported that O_α is more active for soot oxidation than the other two types of oxygen species.[38] Based on the fitted peak areas, the relative ratios of $O_\alpha/(O_\beta + O_\gamma)$ were calculated. With the calcination temperature increasing to 900 °C, the ratio of $O_\alpha/(O_\beta + O_\gamma)$ increased significantly from 0.06 to 0.21, indicating that high-temperature calcination can promote the formation of more surface adsorbed oxygen species.

H_2-TPR was used to analyze the reducibility of the catalysts. Fig. 5b shows the reduction profile of the MnO_x-500 catalyst, which includes four reduction processes. The first reduction peak centered at 269 °C was attributed to the reduction of surface adsorbed oxygen species, and the other three reduction peaks were related to the reduction of MnO_2 to MnO, with Mn_2O_3 and Mn_3O_4 as intermediates.[11,39] Interestingly, when the MnO_x catalyst was calcined at 900 °C, the reduction peak of surface adsorbed oxygen species shifted to a significantly lower temperature (255 °C), which suggested that high-temperature calcination of the catalyst was beneficial to improving the mobility of surface adsorbed oxygen species. Additionally, soot-TPR experiments were also
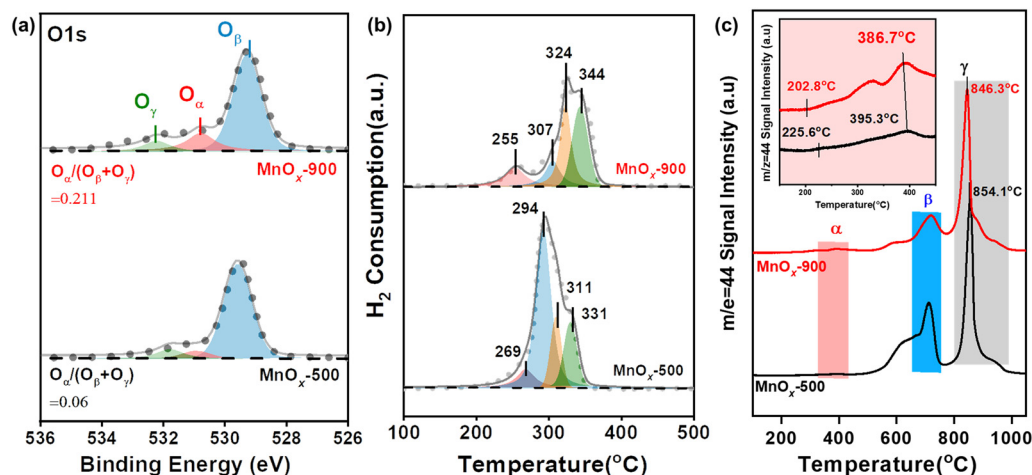
6282 | *Catal. Sci. Technol.*, 2024, **14**, 6278–6285

This journal is © The Royal Society of Chemistry 2024

Fig. 5 O 1s XPS (a), H_2-TPR (b), and soot-TPR (c) results for the MnO_x-900 and MnO_x-500 catalysts.

carried out to further investigate the surface oxygen species of the catalysts, and the results are exhibited in Fig. 5c. The soot-TPR profiles showed three temperature regions, which were associated with the consumption of surface-active oxygen species (<550 °C), surface lattice oxygen (550–750 °C), and bulk lattice oxygen (>690 °C), respectively.[40–43] Considering the temperature range of soot oxidation for the MnO_x-500 and MnO_x-900 catalysts (Fig. 1), the surface-active oxygen species should be the key active oxygen species for soot oxidation. As shown in Fig. 5c, the peak of surface-active oxygen species for the MnO_x-900 catalyst moved towards a lower temperature in comparison with that for MnO_x-500, indicating that the high-temperature calcination could promote the mobility of the surface-active oxygen species, which is consistent with the H_2-TPR results. In addition, MnO_x-900 possessed more surface-active oxygen species than MnO_x-500 (inset in Fig. 5c), which was beneficial for soot oxidation.

3.5 Insight into the effect of calcination temperature

In this work, it was found that with the calcination temperature increasing from 500 to 900 °C, the T_{50} and T_{90} values of the MnO_x catalyst decreased from 394 and 436 °C to 365 and 394 °C, respectively, in the $NO/O_2/N_2$ atmosphere

(Fig. 1b), suggesting that high-temperature calcination enhanced the soot oxidation activity. Structural characterization indicated that high-temperature calcination can induce the formation of δ-MnO_2 and Mn_2O_3 in the MnO_x catalyst, and DFT calculations revealed that oxygen defects are easily formed on δ-MnO_2 and Mn_2O_3. The results of Raman, EPR, and XAFS spectroscopy further confirmed that high-temperature calcination of the catalyst can promote the generation of oxygen defects. The characterization results of O 1s XPS, H_2-TPR and soot-TPR revealed that the generated oxygen defects can facilitate the formation of surface-active oxygen species on the MnO_x catalyst. In addition, the specific activity of NO-to-NO_2 over the MnO_x-500 and MnO_x-900 catalysts in catalytic experiments performed with and without soot (activity normalized by the results of BET), and NO_2 utilization efficiency results (Fig. 1d and S3†) showed that high-temperature calcination had a positive effect on driving NO_2 participation in soot oxidation (NO + O* → NO_2, C + NO_2 → SOCs + NO, SOCs + O* → CO_2/CO, where O* was surface-active oxygen, SOCs were surface oxygen complexes and C represented soot).

Based on the above discussion, the effect of calcination temperature on the soot oxidation activity of MnO_x is schematically shown in Fig. 6. The MnO_x catalyst calcined at high temperature can promote the generation of surface oxygen defects, *via* driving the transformation of α-MnO_2 to δ-MnO_2 and Mn_2O_3. The generated oxygen defects then facilitate the activation of surface chemisorbed oxygen, and the formed active oxygen species further oxidize NO to NO_2 and accelerate soot oxidation. Therefore, MnO_x-900 showed better soot oxidation activity than MnO_x-500.

4. Conclusions

In this study, it was remarkably found that a MnO_x catalyst calcinated at high temperature (900 °C) exhibited better soot oxidation activity than that calcined at low temperature (500 °C). The results of characterization and DFT calculations
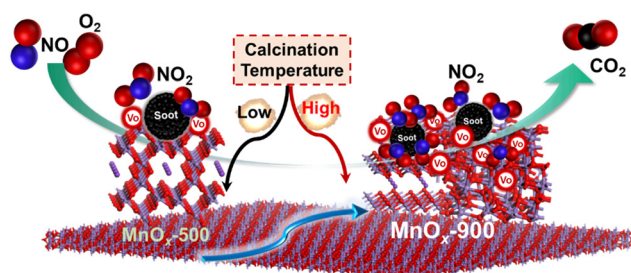

Fig. 6 Schematic illustration of the soot oxidation process of the samples.

This journal is © The Royal Society of Chemistry 2024

Catal. Sci. Technol., 2024, **14**, 6278–6285 | **6283**

revealed that the MnO$_x$-900 catalyst possessed more oxygen defects than MnO$_x$-500, which promoted the formation of surface-active oxygen species and then enhanced the NO$_2$ utilization efficiency for soot oxidation. Therefore, the high-temperature calcination endowed the MnO$_x$ catalyst with superior soot oxidation activity. This work provides significant insight into the effects of calcination temperature on soot oxidation catalysts.

Data availability

All data are incorporated into this article and its online ESI† material: the data underlying this article are available in the article in its online ESI† material.

Conflicts of interest

There are no conflicts to declare.

Acknowledgements

Notes and references

1 P. Zhang, X. Mei, X. Zhao, J. Xiong, Y. Li, Z. Zhao and Y. Wei, Boosting catalytic purification of soot particles over double perovskite-type La$_{2-x}$K$_x$NiCoO$_6$ catalysts with an ordered macroporous structure, *Environ. Sci. Technol.*, 2021, **55**, 11245–11254.

2 M. Wang, Y. Zhang, Y. Yu, W. Shan and H. He, Synergistic effects of multicomponents produce outstanding soot oxidation activity in a Cs/Co/MnO$_x$ catalyst, *Environ. Sci. Technol.*, 2021, **55**, 240–248.

3 X. Mei, X. Zhu, Y. Zhang, Z. Zhang, Z. Zhong, Y. Xin and J. Zhang, Decreasing the catalytic ignition temperature of diesel soot using electrified conductive oxide catalysts, *Nat. Catal.*, 2021, **4**, 1002–1011.

4 Y. Wei, P. Zhang, J. Xiong, Q. Yu, Q. Wu, Z. Zhao and J. Liu, SO$_2$-tolerant catalytic removal of soot particles over 3D ordered macroporous Al$_2$O$_3$-supported binary Pt-Co oxide catalysts, *Environ. Sci. Technol.*, 2020, **54**, 6947–6956.

5 H. Xu, N. Yan, Z. Qu, W. Liu, J. Mei, W. Huang and S. Zhao, Gaseous heterogeneous catalytic reactions over Mn-based oxides for environmental applications: A critical review, *Environ. Sci. Technol.*, 2017, **51**, 8879–8892.

6 Y. Li, P. Zhang, J. Xiong, Y. Wei, H. Chi, Y. Zhang, K. Lai, Z. Zhao and J. Deng, Facilitating catalytic purification of auto-exhaust carbon particles via the Fe$_2$O$_3$\{113\} facet-dependent effect in Pt/Fe$_2$O$_3$ catalysts, *Environ. Sci. Technol.*, 2021, **55**, 16153–16162.

7 I. Atribak, A. Bueno-López, A. García-García, P. Navarro, D. Frías and M. Montes, Catalytic activity for soot combustion of birnessite and cryptomelane, *Appl. Catal., B*, 2010, **93**, 267–273.

8 H. Zhang, Z. Hou, Y. Zhu, J. Wang and Y. Chen, Sulfur deactivation mechanism of Pt/MnO$_x$–CeO$_2$ for soot oxidation: Surface property study, *Appl. Surf. Sci.*, 2017, **396**, 560–565.

9 W. Ren, T. Ding, Y. Yang, L. Xing, Q. Cheng, D. Zhao, Z. Zhang, Q. Li, J. Zhang, L. Zheng, Z. Jiang and X. Li, Identifying oxygen activation/oxidation sites for efficient soot combustion over silver catalysts interacted with nanoflower-like hydrotalcite-derived CoAlO metal oxides, *ACS Catal.*, 2019, **9**, 8772–8784.

10 S. Liu, X. Wu, D. Weng, M. Li and R. Ran, Roles of Acid Sites on Pt/H-ZSM5 Catalyst in Catalytic Oxidation of Diesel soot, *ACS Catal.*, 2015, **5**, 909–919.

11 H. Deng, S. Kang, J. Ma, C. Zhang and H. He, Silver incorporated into cryptomelane-type manganese oxide boosts the catalytic oxidation of benzene, *Appl. Catal., B*, 2018, **239**, 214–222.

12 C. Wang, H. Yuan, G. Lu and H. Wang, Oxygen vacancies and alkaline metal boost CeO$_2$ catalyst for enhanced soot combustion activity: A first-principles evidence, *Appl. Catal., B*, 2021, **281**, 119468.

13 T. Liu, Q. Li, Y. Xin, Z. Zhang, X. Tang, L. Zheng and P. Gao, Quasi free K cations confined in hollandite-type tunnels for catalytic solid (catalyst)-solid (reactant) oxidation reactions, *Appl. Catal., B*, 2018, **232**, 108–116.

14 Y. Yang, D. Zhao, Z. Gao, Y. Tian, T. Ding, J. Zhang, Z. Jiang and X. Li, Interface interaction induced oxygen activation of cactus-like Co$_3$O$_4$/OMS-2 nanorod catalysts in situ grown on monolithic cordierite for diesel soot combustion, *Appl. Catal., B*, 2021, **286**, 119932.

15 D. Jampaiah, V. Velisoju, P. Venkataswamy, V. Coyle, A. Nafady, B. M. Reddy and S. Bhargava, Nanowire morphology of mono- and bidoped α-MnO$_2$ catalysts for remarkable enhancement in soot oxidation, *ACS Appl. Mater. Interfaces*, 2017, **9**, 32652–32666.

16 D. Yu, D. Ren, X. Yu, X. Fan, L. Wang, R. Wang, Z. Zhao, K. Cheng, Y. Chen, Z. Sojka, A. Kotarba, Y. Wei and J. Liu, Facile synthesis of birnessite-type K$_2$Mn$_4$O$_8$ and cryptomelane-type K$_{2-x}$Mn$_8$O$_{16}$ catalysts and their excellent catalytic performance for soot combustion with high resistance to H$_2$O and SO$_2$, *Appl. Catal., B*, 2021, **285**, 119779.

17 M. Hu, K. Zhou, T. Zhao, Z. Li, X. Zeng, D. Yu, X. Yu, M. Zhao, Z. Shao, Q. Xu and B. Cui, Facile preparation and efficient Mn$_x$Co$_y$ porous nanosheets for the sustainable catalytic process of soot, *Green Energy Environ.*, 2024, **9**, 516–528.

18 D. Yan, J. Chen and H. Jia, Temperature-induced structure reconstruction to prepare a thermally stable single-atom platinum catalyst, *Angew. Chem., Int. Ed.*, 2020, **59**, 13562–13567.

19 H. Deng, Y. Lu, T. Pan, L. Wang, C. Zhang and H. He, Metals incorporated into OMS-2 lattice create flexible catalysts with highly efficient activity in VOCs combustion, *Appl. Catal., B*, 2023, **320**, 121955.

6284 | *Catal. Sci. Technol.*, 2024, **14**, 6278–6285

This journal is © The Royal Society of Chemistry 2024

20 W. Yang, Z. A. Su, Z. Xu, W. Yang, Y. Peng and J. Li, Comparative study of α-, β-, γ- and δ-MnO$_2$ on toluene oxidation: Oxygen vacancies and reaction intermediates, *Appl. Catal., B*, 2020, **260**, 118150.

21 J. Zhang, Y. Li, L. Wang, C. Zhang and H. He, Catalytic oxidation of formaldehyde over manganese oxides with different crystal structures, *Catal. Sci. Technol.*, 2015, **5**, 2305–2313.

22 T. Hamaguchi, T. Tanaka, N. Takahashi, Y. Tsukamoto, N. Takagi and H. Shinjoh, Low-temperature NO-adsorption properties of manganese oxide octahedral molecular sieves with different potassium content, *Appl. Catal., B*, 2016, **193**, 234–239.

23 J. Luo, Q. Zhang, J. Garcia-Martinez and S. Suib, Adsorptive and acidic properties, reversible lattice oxygen evolution, and catalytic mechanism of cryptomelane-Type manganese oxides as oxidation catalysts, *J. Am. Chem. Soc.*, 2008, **130**, 3198–3207.

24 X. Li, J. Ma and H. He, Tuning the chemical state of silver on Ag-Mn catalysts to enhance the ozone decomposition performance, *Environ. Sci. Technol.*, 2020, **54**, 11566–11575.

25 L. Yang, J. Ma, X. Li, C. Zhang and H. He, Enhancing oxygen vacancies of Ce-OMS-2 via optimized hydrothermal conditions to improve catalytic ozone decomposition, *Ind. Eng. Chem. Res.*, 2019, **59**, 118–128.

26 G. Zhu, J. Zhu, W. Jiang, Z. Zhang, J. Wang, Y. Zhu and Q. Zhang, Surface oxygen vacancy induced α-MnO$_2$ nanofiber for highly efficient ozone elimination, *Appl. Catal., B*, 2017, **209**, 729–737.

27 Y. Zheng, Y. Su, C. Pang, L. Yang, C. Song, N. Ji, D. Ma, X. Lu, R. Han and Q. Liu, Interface-enhanced oxygen vacancies of CoCuO$_x$ Catalysts in situ grown on monolithic Cu foam for VOC catalytic oxidation, *Environ. Sci. Technol.*, 2022, **56**, 1905–1916.

28 S. Rong, P. Zhang, F. Liu and Y. Yang, Engineering crystal facet of α-MnO$_2$ nanowire for highly efficient catalytic oxidation of carcinogenic airborne formaldehyde, *ACS Catal.*, 2018, **8**, 3435–3446.

29 Y. Zheng, K. Fu, Z. Yu, Y. Su, R. Han and Q. Liu, Oxygen vacancies in a catalyst for VOCs oxidation: synthesis, characterization, and catalytic effects, *J. Mater. Chem. A*, 2022, **10**, 14171–14186.

30 Y. Lu, H. Deng, T. Pan, L. Wang, C. Zhang and H. He, Interaction between noble metals (Pt, Pd, Rh, Ir, Ag) and defect-enriched TiO$_2$ and its application in toluene and propene catalytic oxidation, *Appl. Surf. Sci.*, 2022, **606**, 154834.

31 A. Jia, Y. Zhang, T. Song, Z. Zhang, C. Tang, Y. Hu, W. Zheng, M. Luo, J. Lu and W. Huang, Crystal-plane effects of anatase TiO$_2$ on the selective hydrogenation of crotonaldehyde over Ir/TiO$_2$ catalysts, *J. Catal.*, 2021, **395**, 10–22.

32 S. Mo, Q. Zhang, J. Li, Y. Sun, Q. Ren, S. Zou, Q. Zhang, J. Lu, M. Fu, D. Mo, J. Wu, H. Huang and D. Ye, Highly efficient mesoporous MnO$_2$ catalysts for the total toluene oxidation: Oxygen-vacancy defect engineering and involved intermediates using in situ DRIFTS, *Appl. Catal., B*, 2020, **264**, 118464.

33 J. Ma, C. Wang and H. He, Transition metal doped cryptomelane-type manganese oxide catalysts for ozone decomposition, *Appl. Catal., B*, 2017, **201**, 503–510.

34 C. Wang, J. Ma, F. Liu, H. He and R. Zhang, The effects of Mn^{2+} precursors on the structure and ozone decomposition activity of cryptomelane-type manganese oxide (OMS-2) catalysts, *J. Phys. Chem. C*, 2015, **119**, 23119–23126.

35 X. Li, J. Ma, L. Yang, G. He, C. Zhang, R. Zhang and H. He, Oxygen vacancies induced by transition metal doping in gamma-MnO$_2$ for highly efficient ozone decomposition, *Environ. Sci. Technol.*, 2018, **52**, 12685–12696.

36 Y. Wang, J. Wu, G. Wang, D. Yang, T. Ishihara and L. Guo, Oxygen vacancy engineering in Fe doped akhtenskite-type MnO$_2$ for low-temperature toluene oxidation, *Appl. Catal., B*, 2021, **285**, 119873.

37 X. Lin, S. Li, H. He, Z. Wu, J. Wu, L. Chen, D. Ye and M. Fu, Evolution of oxygen vacancies in MnO$_x$-CeO$_2$ mixed oxides for soot oxidation, *Appl. Catal., B*, 2018, **223**, 91–102.

38 P. Zhang, M. Yang, D. Han, X. Liu, X. Yu, J. Xiong, Y. Li, Z. Zhao, J. Liu and Y. Wei, Activating well-defined α-Fe$_2$O$_3$ nanocatalysts by near-surface Mn atom functionality for auto-exhaust soot purification, *Appl. Catal., B*, 2023, **321**, 122077.

39 J. Ji, X. Lu, C. Chen, M. He and H. Huang, Potassium-modulated δ-MnO$_2$ as robust catalysts for formaldehyde oxidation at room temperature, *Appl. Catal., B*, 2020, **260**, 118210.

40 M. Zhao, J. Deng, J. Liu, Y. Li, J. Liu, Z. Duan, J. Xiong, Z. Zhao, Y. Wei, W. Song and Y. Sun, Roles of surface-active oxygen species on 3DOM cobalt-based spinel catalysts M$_x$-Co$_{3-x}$O$_4$ (M = Zn and Ni) for NO$_x$-assisted soot oxidation, *ACS Catal.*, 2019, **9**, 7548–7567.

41 C. Cao, L. Xing, Y. Yang, Y. Tian, T. Ding, J. Zhang, T. Hu, L. Zheng and X. Li, Diesel soot elimination over potassium-promoted Co$_3$O$_4$ nanowires monolithic catalysts under gravitation contact mode, *Appl. Catal., B*, 2017, **218**, 32–45.

42 B. Jin, B. Zhao, S. Liu, Z. Li, K. Li, R. Ran, Z. Si, D. Weng and X. Wu, SmMn$_2$O$_5$ catalysts modified with silver for soot oxidation: Dispersion of silver and distortion of mullite, *Appl. Catal., B*, 2020, **273**, 119058.

43 X. Feng, J. Xu, X. Xu, S. Zhang, J. Ma, X. Fang and X. Wang, Unraveling the principles of lattice disorder degree of Bi$_2$B$_2$O$_7$ (B = Sn, Ti, Zr) compounds on activating gas phase O$_2$ for soot combustion, *ACS Catal.*, 2021, **11**, 12112–12122.

This journal is © The Royal Society of Chemistry 2024

Catal. Sci. Technol., 2024, **14**, 6278–6285 | **6285**